Article Information

Article Type:	Research Article
Section Heading:	
Journal Title:	Journal of Sustainable Cement-Based Materials
Publisher:	Taylor & Francis
DOI Number:	10.1080/21650373.2025.2537266
Volume Number:	0
Issue Number:	0
First Page:	1
Last Page:	19
Copyright:	
Copyright Holder:	Informa UK Limited, trading as Taylor & Francis Group
License:	
Received Date:	2025-4-30
Accepted Date:	2025-7-17

Alkaline-activated cements synthesized from spent diatomaceous earth and different industrial sludge ashes

AQ0

M. Felipe-Sesé[a], A. García-Díaz[b], M. A. Gómez-Casero[b,c] and D. Eliche-Quesada[b,c] AQ1

[a]ESIT – Escuela Superior de Ingeniería y Tecnología, Universidad Internacional de La Rioja, Logroño, Spain;

[b]Department of Chemical, Environmental and Materials Engineering, Higher Polytechnic School of Jaén, University of Jaén, Jaén, Spain;

[c]Center for Advanced Studies in Earth Sciences, Energy and Environment (CEACTEMA), University of Jaén, Jaén, Spain

Footnotes

No author footnotes is available

Corresponding Author

Corresponding author. Email: deliche@ujaen.es Department of Chemical, Environmental and Materials Engineering, Higher Polytechnic School of Jaén, University of Jaén, Campus Las Lagunillas, 23071 Jaén, Spain; Center for Advanced Studies in Earth Sciences, Energy and Environment (CEACTEMA), University of Jaén, Campus Las Lagunillas s/n, 23071 Jaén, Spain

This study evaluates the technological properties of alkali-activated cements (AACs) produced from spent diatomaceous earth (SDE), a by-product of beer filtration, combined with 20 wt.% of industrial

sludge ashes. The ashes used include brewery sludge ash (BSA), oil industry sludge ash (OSA), pulp–paper sludge ash (PSA), and aluminum anodizing sludge ash (AASA). Activation was carried out using a 1:1 mixture of sodium silicate and sodium hydroxide, with curing at room temperature for 7 and 28 days. Microstructural analysis was performed using X-ray diffractometer (XRD), Fourier transform infrared (FTIR) spectroscopy, scanning electron microscopy (SEM), and scanning electron microscopy with energy dispersive X-ray spectroscopy (SEM-EDS). The results show that the chemical composition of the sludge ashes significantly influences the mechanical performance of AACs. Calcium-rich wastes improved compressive strength, while the presence of SO_3 and P_2O_5 reduced it due to the formation of expansive phases or secondary reactions. The best results were achieved with BSA-SDE cements, which reached compressive and flexural strengths of 30.0 and 6.5 MPa, respectively.

Keywords

Sludge ash; alkali-activated cements; spent diatomaceous earth; mechanical properties; geopolymers; microstructure

This research has been funded by the project Activalo2: Valorisation of Urban and Industrial Wastewater Treatment Sludge in the Manufacture of New Sustainable Alkaline Activated Materials for a Circular Economy (UJA-1380933) Proyectos de I + D + i en el marco del Programa Operativo FEDER Andalucía 2014–2020.

1. Introduction

Concrete, the second-most consumed substance on Earth, is an essential part of any building or structure and the most popular construction material, which contains cement as a fundamental component. Cement production is the third-largest CO_2-emitting industry globally, accounting for 5% of all CO_2 emissions [1]. Almost all types of cement are made with Portland cement manufactured by heating significant amounts of natural resources, clay (or shale), and limestone (or chalk) in cement processing plants. A substantial share of CO_2 emissions, ranging from 50% to 60%, originates from the decomposition of limestone ($CaCO_3$), while 30–40% is produced by the combustion of fossil fuels during the heating processes. The remaining emissions result from electricity use in air coolers

and mills [2]. Considering current technology, producing 1 ton of Portland cement releases 1 kg of SO_2, 2 kg of NO_x, 10 kg of dust, and nearly 640 kg of CO_2 into the atmosphere [3].

The continuous increase of CO_2 in the atmosphere and the devastating impacts of global warming have driven a surge in research on alternative, more environmentally sustainable materials aimed at reducing CO_2 emissions in the cement industry. Alkali-activated cements (AACs), also called geopolymers (mainly for systems with low calcium content), a class of inorganic materials, are examples of promising cementitious products that can partially substitute Portland cement. AAC are synthesized from raw materials containing amorphous silica (SiO_2), alumina (Al_2O_3) and high or low calcium content (CaO) together with an alkaline activator [4]. Manufacturing AACs enables the use of different industrial wastes as raw materials, reducing the usage of natural resources, avoiding landfill disposal, and reducing CO_2 emissions by 80% [5].

Alkaline activation or geopolymerization is a chemical reaction that can be produced in the temperature range of 20–100 °C. On the one hand, AACs obtained from materials rich in silica, aluminum, and calcium produce a cementitious material, a C–(A)–S–H gel, similar to Portland cement, although with a certain aluminum content in its structure. Linear chains of silica tetrahedra form this gel. On the other hand, AACs obtained from raw materials rich in silicon and aluminum, the main reaction product is an N–A–S–H geopolymeric gel. This gel has a 3D structure resulting from the dissolution of aluminosilicate-type materials in the alkaline medium and the formation of oligomers, $Si(OH)^{4-}$ and $Al(OH)^{4-}$ together with hydroxylated compounds that, during the polycondensation reaction, give rise to tetrahedral units which form an amorphous 3D network [4,6].

Among the advantages of AACs include the following: they are low-priced; they can harden in very little time at ambient temperatures similar to fast cement but with improved physical properties [7]; their structure does not oxidize or decompose under high temperatures (1000–1200 °C); and they have excellent heat insulation properties, good mechanical characteristics, exhibit excellent acid resistance and lower shrinkage compared with cement [3,7–14]. It has even been shown to have better resistance properties in certain applications, such as in marine environments [15]. In this regard, it is also worth noting that alkali-activated binders have been widely explored for the

stabilization of soil-like materials, particularly expansive clays such as black cotton soil. The incorporation of fly ash, rice husk ash (RHA), red mud, and other industrial by-products in combination with alkaline activators has been shown to significantly improve mechanical strength, durability, and reduce leaching of contaminants, making these systems promising alternatives in geotechnical and pavement applications [16–20]. These findings further support the feasibility of valorizing industrial sludges with soil-like characteristics as precursors in alkali-activated systems.

However, the composition of the precursors determines the properties of AACs. Due to environmental concerns, studying the use of industrial waste as an adequate and sustainable alternative to conventional raw materials (metakaolin) is especially relevant, as it additionally helps to avoid the overexploitation of natural resources.

Spent diatomite earth (SDE) is an industrial by-product composed of diatom, yeast, and other organic matter restrained in the filtration phase of the beer manufacturing process [20]. Diatomite is a biogenic sedimentary rock formed by the accumulation of siliceous shells of unicellular organisms, particularly diatoms, and it presents a high content of natural amorphous silica [21]. Due to its unique porous structures, high adsorption capacity, and low density [22], diatomite is widely used as a filtration material. One liter of clarified beer consumes approximately 1–2 g of diatomite, generating 17.14 g of spent diatomite [23]. This waste is reused in different fields, highlighting its use as a building material, as shown in the following studies: concrete made with brewery-spent diatomite [24]; concrete with variable loadings of diatomite [25,26]; clay-based materials with spent diatomite [27]. Other applications of SDE have been studied, such as those in the chemical industry and water treatment: preparing high-performance photocatalysts [28]; removing fluoride from drinking water using brewery waste diatomite [29]. Regeneration methods of spent diatomite have also been studied [23,30]. It might be pointed out that applying this residue in agriculture as organic fertilizer is controversial, as it can lead to soil contamination [31]. At present, only small amounts of spent diatomite are reused, and large quantities are disposed of in landfills, occupying vast land, and releasing CO and CO_2 into the atmosphere. SDE, however, is rich in amorphous silica and has a high surface area, which makes it a promising precursor for the manufacture of AACs, although it has been little explored in this context [32,33].

Another type of waste generated in large quantities is wastewater treatment sludge. In Spain, around 1.2 million tons (in dry matter) of sludge from wastewater treatment plants are produced annually [34] and the trend is to increase. In 2022, approximately 81.7% of the sludge produced in Spain was reused in agriculture, forestry and gardening if its heavy metal content is adequate. A 7.9% of its final use was energy use or incineration, generating ash as waste. It must be considered that 10.3% of the total was deposited in landfills [35]. It is evident that the composition and characteristics of the sludge generated by the treatment of industrial wastewater vary considerably depending on the type of industry that produces it. However, sludge ashes resulting from the incineration of industrial wastewater treatment sludge often contain significant amounts of alumina, calcium, and silica and other oxides depending on their origin. These chemical characteristics make them suitable for use as complementary precursors in alkali-activated matrices contributing to gel formation and improving mechanical performance.

Brewery sludge (BS) is a residue resulting from wastewater treatment plants at different stages of the brewing process. Around 14–20 kg of BS is obtained per hectoliter of beer produced [36]. It is mainly composed of organic matter and essential nutrients with great potential as fertilizer in agriculture [37–39], considering the limitations on the use due to the heavy metals concentrations and presence of pathogens [40,41], alternative uses of this type of waste have been studied. One example is its use as a source of energy and the subsequent utilization of its ashes in the construction sector: BS as an energy source and its ashes as an additive for the cement industry [40]; geopolymer concrete materials made with brewery sludge ash (BSA) [41]; lightweight aggregates manufactured with clay and wastes from the brewing industry [42]. Other studies have researched the potential recovery of components of the BS and sub-products: recovery of water, nitrogen, and carbon from brewery effluent [43] and of methane between algal and activated BS as a result of anaerobic digestion [44].

Oil industry sludge (OS) is an aqueous waste from vegetable oil extraction and refining. It is mainly composed of organic matter and mineral compounds. In the case of the oil industry, traditional methods of oil sludge disposal consisted of ocean discharge and incineration. However, nowadays, these sludges are mainly used to amend agricultural soil. It must be taken into account that this

practice may constitute a risk due to the residue's possible antimicrobial and phytotoxic effects that might increase salinity and nitrogen immobilization [45]. Composting this sludge is proposed as the environmentally most beneficial way of extracting agricultural value from it [46]. Currently, other applications for this sludge are under study, as shown in the following research publications: sludge from the olive oil industry as an adsorbent for the removal of water contaminants [47,48]; biomethane recovery from olive mill residues through anaerobic digestion [49]; residues from olive oil production for manufacturing ceramic materials or alkaline activated cements materials [50–53].

Pulp–paper industry sludge (PS) is a by-product resulting from wastewater treatment in the paper and cellulose industry, and it is characterized by its high humidity, approximately, 50% of water content, and its composition, mainly basic kaolin and cellulose along with other materials in small amounts, including heavy metals. The paper and cellulose industry is growing at annual rates of up to 30% worldwide. It should be considered that for every ton of paper produced, around 400 kg of residue is generated [54]. Although paper–pulp industry sludge is classified as a non-hazardous material due to the fraction of metal being not significant, typically, this waste is disposed of in landfills with the consequent economic cost and environmental impact on soil and groundwater [55]. Different solutions have been proposed to reuse this sludge, considering the high concentration of cellulose fibers as an advantage to be used as reinforcement components in building materials, improving their technological properties [56]. At the same time, incorporating the sludge into ceramic materials has contributed to substantially reducing dumping [57]. The following recent research shows the advantages of incorporating this by-product in different construction materials: calcium silicate board materials [58]; green geopolymer mortars [59]; soil-cement blocks [60]; and cement-based mortars [55]. Likewise, other uses of this sludge were studied, such as the case of soil stabilization and correction [57].

Aluminum anodizing industry sludge (AAS) is a by-product of chemical treatment that provides anticorrosion protection to aluminum. Due to its high alkalinity, the sludge is classified as hazardous. According to the International Aluminium Institute, demand for aluminum products has doubled since 2000. Worldwide aluminum production was 88,383 thousand metric tons in 2023 [61], and an estimated 1 ton of sludge is generated for each ton of anodized material. The large quantity of

hazardous waste produced globally creates a significant environmental impact and requires the search for new possibilities for recycling [62]. In this regard, the possible uses of AAS as building material have been studied as stated in the following research articles: composites of construction materials, mortar-cement, and lime waste [62,63]; environmentally clean composites produced with iron ore processing tailings, ASA, concrete waste, and lime production waste [64]; boards with flame resistance made with recycled PET and AAS [65]; bricks fired with AAS and clay bricks [66]; and RHA and ASA as precursors for the synthesis of geopolymers [67].

In view of the above, the management of industrial wastewater sludge represents an important challenge for companies due to the growing environmental concerns and demands, making clear the need to seek new innovative waste recovery processes that comply with the current legislation.

The combined use of BDS and sludge ash from different industries in AAC formulations can offer synergistic effects by complementing each other in terms of chemical composition, supporting circular economy strategies and providing a sustainable outlet for waste that is often landfilled, thus mitigating its environmental impact.

In this research, the manufacture of AACs is proposed by using spent diatomaceous earth (SDE) from the brewing industry in combination with each of the ashes resulting from the combustion of wastewater treatment sludge generated in the following sectors: brewing, vegetable oil refining, pulp–paper manufacturing, and aluminum anodizing. The materials obtained were cured at ambient temperature, and afterwards, the physical, mechanical, and microstructural properties of the new conglomerates produced were studied.

This work is the first comparative study that explores the combined use of BDS and different industrial sludge ashes as precursors in the synthesis of CAAs. The novelty of the research lies not only in the joint valorization of two little exploited industrial wastes, but also in the systematic analysis of the effect of the chemical composition of each ash on the type of gels formed during activation, as well as on the microstructure and mechanical performance of the final binder.

2. Materials and methods

2.1. Raw materials and characterization

The SDE, together with BS, was supplied by the company Heineken S.L., from a brewery situated in Jaén (Spain). The OS was provided by the oil and fat refining company Aceites del Sur Coosur, S.A. (Vilches, Jaén, Spain). The aluminum anodizing sludge (AAS) was supplied from Alusistemas S.A. (Mancha Real, Jaén, Spain), an anodizing plant. With respect to the PS, it was provided by the Cotton South S.L. Celsur Company (Fonelas, Spain).

All raw materials were dried at 100 °C until a constant mass was achieved. The by-products were then subjected to the corresponding calcination. The calcination of those precursors is necessary in order to avoid the presence of organic matter which causes a delayed formation of the main hydrated products, with a consequential negative effect on the setting and mechanical properties. In addition, the calcination of the organic matter improves the precursor's reactivity, contributing to the pozzolanic activity. The temperature and calcination time parameters were previously established by thermogravimetric analysis and differential thermal analysis (TGA–DTA) tests (Figure 1). These tests made it possible to determine the optimal conditions to guarantee the complete decomposition of the organic matter contained in the raw materials. SDE was calcined at 600 °C, while BS, OS, and PS were calcined at 800 °C, and AAS at 400 °C, for a duration of 2 h, with a heating rate of 10 °C/min. Following calcination, the materials underwent milling in a ball mill for 30 min at a rotational speed of 350 rpm. Subsequently, they were sieved to achieve a particle size of less than 100 µm. The materials obtained were called: SDE, aluminum anodizing sludge ash (AASA), BSA, oil sludge ash (OSA), and pulp–paper sludge ash (PSA).

Figure 1. Thermogravimetric and differential thermal analysis (TGA–DTA). (a) SDE, (b) PS, (c) BS, (d) AAS, and (e) OS.

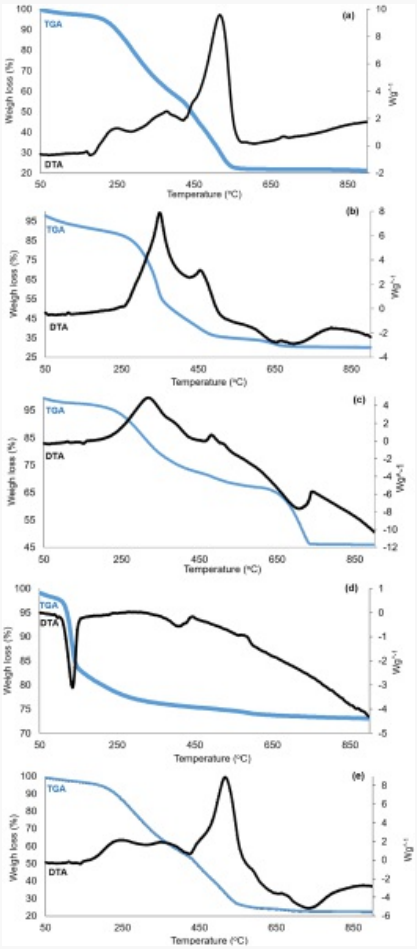

The particle size distribution of the calcined precursors was determined by laser diffraction analysis. To this end, a Malvern Mastersizer 2000 laser diffractometer (Malvern, UK) was used. The particle size distribution of the calcined precursors is shown in Figure 2 and it differs considerably between raw materials. The Dv50 value is significantly higher in the case of OSA, with a value of 66.9 µm. PSA (Dv50 = 10.9 µm) is followed by a difference close to SDE (Dv50 = 7.78 µm). With lower and close values are AASA (Dv50 = 4.47 µm) and BSA (Dv50 = 3.11 µm).

Figure 2. Particle size distribution of precursors.

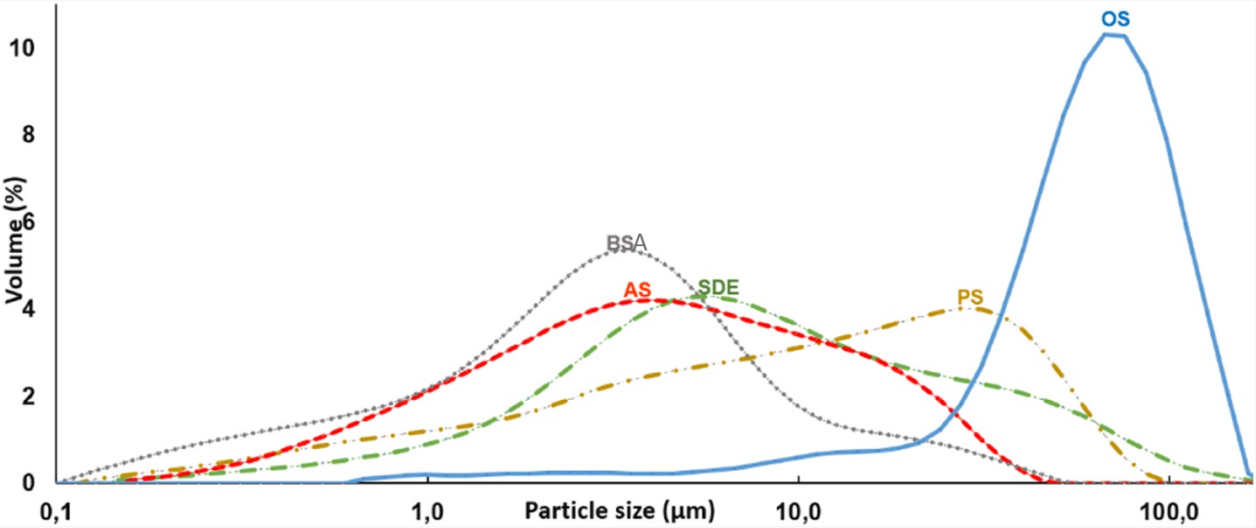

The mineralogical phase analysis of the raw materials was conducted in the 10–80° 2θ range, with a step size of 0.02°, using an Empyrean X-ray diffractometer (XRD) equipped with a PIXcel-3D detector from PANalytical. The analysis was performed using Cu Kα radiation (λ = 1.5406 Å) at a voltage of 40 kV and a current of 40 mA. The resulting XRD diffractograms were processed and analyzed using HighScore software. The main inorganic crystalline phases identified in the XRD patterns are the following (Figure 3): SDE, raw material calcined, presented α-cristobalite and α-quartz as major constituents, with sanidine present in minor proportions [25]; PSA, calcite, periclase (MgO), larnite (Ca_2SiO_4), and portlandite ($Ca(OH)_2$) (and cellulose) [68,69]; BSA, calcite ($CaCO_3$), basanite ($2CaSO_4{\cdot}H_2O$), and merwinite ($Ca_3Mg(SiO_4)_2$) [25,70]; AASA, lime ($Ca(OH)_2$), anhydrite ($CaSO_4$), and millosevichite ($Al_2(SO_4)_3$; OSA, berlinite ($AlPO_4$) mainly.

Figure 3. XRD spectrum of precursors: (a) SDE, (b) PSA, (c) BSA, (d) AASA, and (e) OSA.

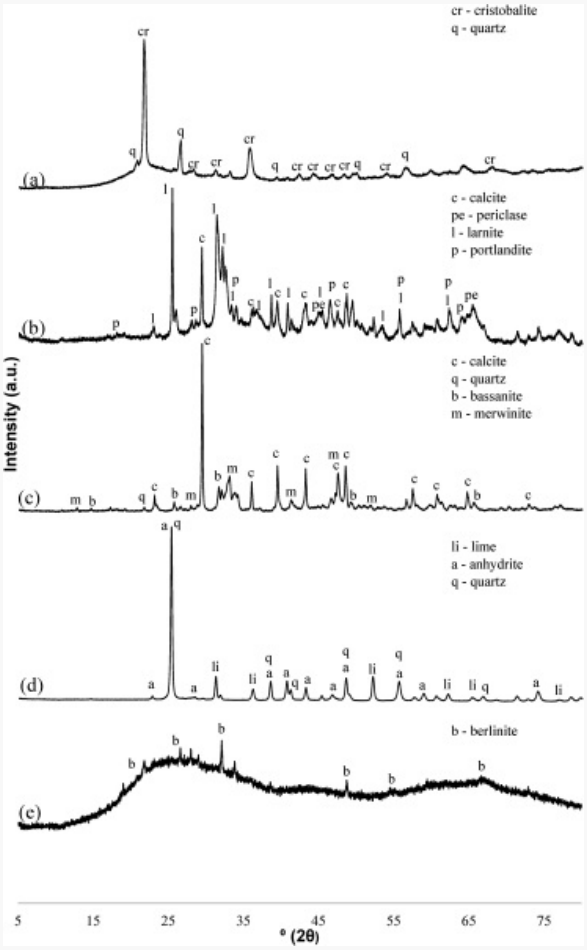

The chemical composition of the raw materials was analyzed by X-ray fluorescence (XRF) using a Philips Magix Pro model PW-2440 instrument (Amsterdam, Netherlands). The results of the analysis are presented in Table 1. The SDE residue is predominantly composed of SiO_2 (89.09%), with smaller quantities of Al_2O_3 (3.22%), Fe_2O_3 (2.72%), and CaO (1.21%). PSA includes as primary components, Al_2O_3 (32.33%) and CaO (29.52%), with significant amounts of P_2O_5 (13.17%), MgO (8.06%), and SO_3 (7.94%). The main components of BSA are CaO (59.36%) and SiO_2 (22.41%); AASA, the mayor components are CaO (34.96%) and SO_3 (32.94%) followed by Al_2O_3 (21.51%).

OSA contains mainly Al_2O_3 (62.04%) and to a lesser extent P_2O_5 (18.13%) and Na_2O (6.29%).

Note: The table layout displayed in 'Edit' view is not how it will appear in the printed/pdf version. This html display is to enable content corrections to the table. To preview the printed/pdf presentation of the table, please view the 'PDF' tab.

Table 1. Chemical (wt.%) composition of the raw materials.

Raw material	SiO_2	Al_2O_3	Fe_2O_3	CaO	MgO	Na_2O	K_2O	P_2O_5	SO_3	LOI[a]
SDE	89.09	3.22	2.72	1.21	0.42	1.35	0.22	0.47	0.09	0.41
PSA	2.83	32.33	0.41	29.52	8.06	2.76	0.1	13.17	7.94	4.07
BSA	21.41	2.98	2.28	55.36	1.49	1.42	0.24	3.38	2.24	7.54
AASA	0.39	21.51	0.14	34.96	0.45	0.89	–	–	32.94	5.12
OSA	2.16	62.04	1.02	3.22	0.52	2.27	0.36	18.13	1.20	8.03

[a]LOI: loss of ignition.

Scanning electron microscopy (SEM) using energy dispersive X-ray spectroscopy (EDS) was employed to examine the morphology of the calcined raw materials (Figure 4). The samples were mounted on an aluminum grid and then coated with a thin layer of carbon using a JEOL JFC 1100 sputter coater (Akishima, Japan).

Figure 4. SEM micrographs of raw materials: (a) SDE, (b) PSA, (c) BSA, (d) AASA, and (e) OSA.

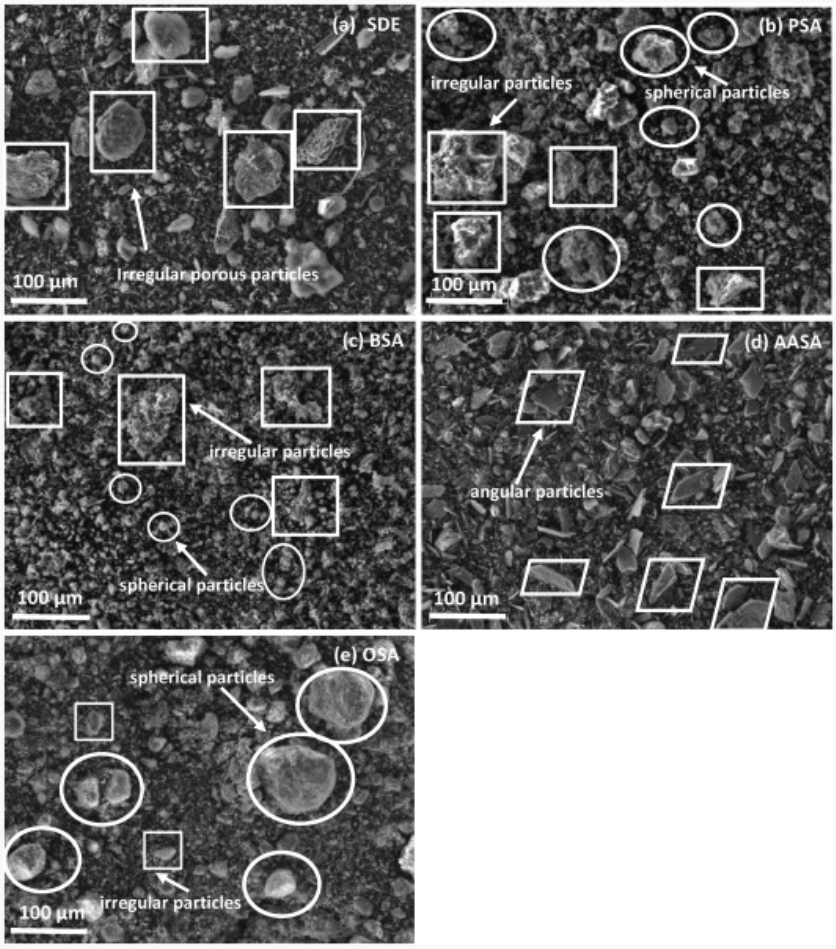

As illustrated in Figure 4, the SDE particles exhibit irregular shapes and a broad range of sizes. The morphology of these particles is characterized by a rough surface texture, with a porous microstructure that is likely to enhance adsorption capacity and increase water demand [71]; BSA, OSA, and PSA show spherical and some irregular shapes particles of a wide variety of sizes, presenting OSA and to a lesser extent PSA larger particle. The particles are porous, allowing BSA, OSA, and PSA to be used as hydraulic mineral additives. Due to the porosity and open areas, coagulated particles are observed. AASA shows smaller angular particles.

Attenuated total reflectance Fourier transform infrared (ATR-FTIR) spectroscopy was carried out in

the range of 4000–400 cm^{-1} using a Vertex 70 Bruker instrument (Billerica, MA) to identify the characteristic functional groups present in the samples (Figure 5). SDE exhibited absorption bands centered at 1069 cm^{-1} and 457 cm^{-1}, which are attributed to the silica absorption bands corresponding to the stretching vibrations of Si–O–Si bonds [33]. The band centered at 794 cm^{-1} is also assigned to Si–O–Si bonds, associated with the presence of amorphous SiO_2 in the waste [72]. A centered band of high intensity between 1036 and 1092 cm^{-1} is observed in all raw materials and it is attributed to the asymmetric stretching vibration of the siloxane group Si–O–Si [73]. The bands observed between 580 cm^{-1} and 620 cm^{-1} correspond to the Al–O bond and Al–OH bond, respectively [67,74]. The absorption peaks at approximately 670 cm^{-1} are attributed to the symmetric stretching vibration of Si–O–Al [75]. AASA, OSA, and PSA samples display absorption bands centered around 3400 cm^{-1} and 1630 cm^{-1}, which are attributed to the O–H stretching and bending vibrations of the O–H–O bonds in water molecules absorbed on the surface of the material [76]. PSA sample shows a prominent peak centered at 1448 cm^{-1}, which is associated with the carbonate ion (CO_3^{2-}), and a band at 872 cm^{-1}, which corresponds to the bending vibration of the carbonyl groups in the SiO_4^{4-} structure, as a result of the presence of larnite [77] and to the existence of inorganic carbonate [78]. The appearance of bands in the range of 600–400 cm^{-1} suggests the presence of Si–O–Si and Al–O–Si bonds, indicating the transition from an amorphous to a semi-crystalline state in the aluminosilicate [68,78].

BSA presents a high band at 1398 and 874 cm^{-1}, corresponding to the carboxyl group stretching absorption peak and the stretching vibrations of C–O [79]. C–H bonds are also observed at 720 cm^{-1}.

The OSA FTIR spectra show two main absorption bands: 1076 cm^{-1}, previously commented, and 463 cm^{-1} assigned to O–Si–O bending [53] (Figure 5). AQ2

Figure 5. FTIR spectra of precursors: (a) SDE, (b) PSA, (c) BSA, (d) AASA, and (e) OSA.

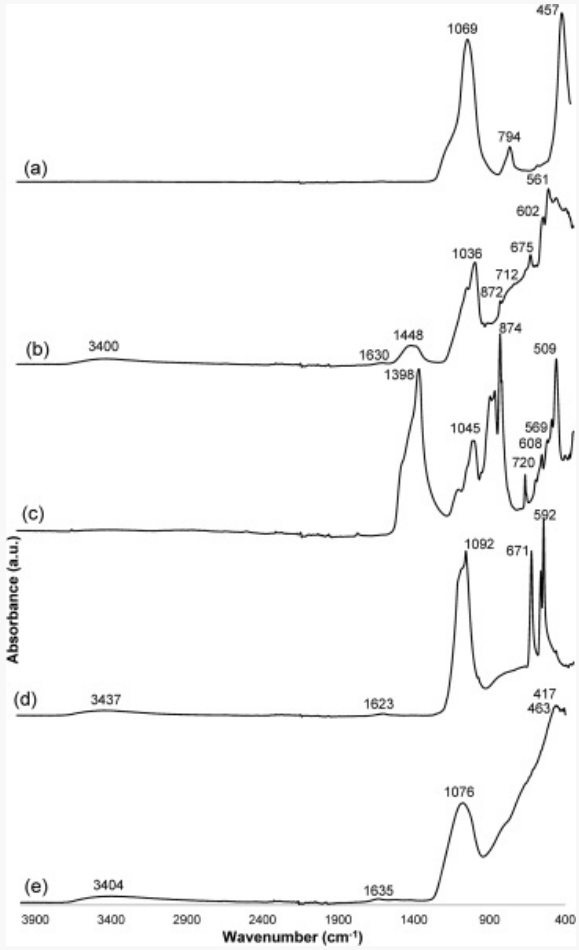

2.2. Synthesis of alkali-activated cements

The first step involves preparing the alkaline activator, with a molar ratio of Ms (mol SiO_2/mol Na_2O) = 1.00, value used in other studies for waste with high silica content [80,81]. This activator consists of a 50 wt.% NaOH 8 M solution (98% purity, Panreac, Barcelona, Spain) and a 50 wt.% Na_2SiO_3 solution, which contains 29.2% SiO_2, 8.9% Na_2O, and 61.9% H_2O. The required amount of NaOH is dissolved in distilled water to achieve an 8 M concentration. This dissolution is exothermic, so the solution must be allowed to cool. Once the 8 M NaOH solution has cooled, it is

weighed, and the appropriate amount of Na_2SiO_3 is added. After homogenizing the solution, the pH is measured using a Crison Basic 20 pH meter. The procedure followed comprised the following steps:

1. *Mixing of precursors*: In the first step, the precursors, each sludge and SDE, were mixed and homogenized for 90 seconds at low speed.
2. *Activating solution*: Subsequently, the commercial activating solution was poured into the homogeneous mixture and the material was homogenized for an additional 90 seconds at low speed. The mixture that had adhered to the walls of the container was scraped off and reintroduced into the bulk. It was then mixed for an additional 30 seconds at high speed.
3. *Molding*: The formed paste was then poured into the 60 × 10 × 10 mm steel molds to conform suitable samples to determine physical and mechanical properties.
4. *Vibration*: The filled molds were subjected to 60 strokes on a Proeti vibrating table (Madrid, Spain) to eliminate any air bubbles and enhance the compaction of the material, ensuring a more uniform and dense final structure.
5. *Curing*: The specimens were covered with a protective film and cured at 22 ± 2 °C, for 24 hours prior to demolding. After demolding, they were kept under the same temperature and relative humidity ≈50% until the specified testing ages of 7 and 28 days.

Table 2 provides information about all prepared samples, which are designated as AASA-SDE, BSA-SDE, OSA-SDE, and PSA-SDE. The proportions of the mixtures utilized in this study remained consistent across all specimens: SDE: 80 wt.% and different sludges ash AASA, BSA, OSA, and PSA: 20 wt.%. The selected dosage of 20 wt.% sludge ash was based on preliminary trials in which replacement levels of 10, 20, and 30 wt.% of SDE were evaluated. A 20 wt.% addition was identified as the optimal compromise, ensuring acceptable workability and compressive strength while maximizing waste valorization. This range is also supported by literature, which considers substitution levels of 10–30 wt.% sludge ash effective in alkali-activated systems [82,83].

Table 2. Mixture compositions of alkaline-activated cements.

Sample	SDE (g)	PSA (g)	BSA (g)	AASA (g)	OSA (g)	NaOH (g)	Na_2SiO_3 (g)	Water in silicate (g)	Total water (g)	*l*/*b*
PSA-SDE	320	80	–	–	–	66.46	270	167.13	203.54	1.35
BSA-SDE	320	–	80	–	–	66.46	270	167.13	203.54	1.35
AASA-SDE	320	–	–	80	–	76.31	310	191.89	233.69	1.55
OSA-SDE	320	–	–	–	80	86.15	350	216.65	263.85	1.75

Place the cursor position on table column and click 'Add New' to add table footnote.

2.3. Experimental methods and characterization of alkali-activated cements

The specimens underwent flexural strength tests in compliance with the UNE-EN 1015-11:2000/A1:2007 standard [84]. Testing was performed using an MTS Insight 5 machine with a 5 kN capacity, operating at a displacement speed of 0.2 mm/min. A total of five samples from each composition and curing time were tested. The flexural strength (σF) was calculated using the following equation:

$$\sigma_F = 1.5\frac{Fl}{bd^2}$$

where F is the applied load in N, l is the span, defined as the distance between the axes of the support rollers (mm), b is the width of the specimen (mm), and d is the thickness of the specimen (mm).

Upon fracture of the specimens during the bending test, each specimen is divided into two parts. One half is utilized for the subsequent compression test, while the other half is reserved for the determination of bulk density.

The compressive strength of five half specimens was measured in accordance with the UNE-EN 1015-11:2000/A1:2007 standard [84]. The test was performed using the MTS 8101 universal testing machine with a capacity of 100 kN. The compressive strength was determined using the following equation:

$$\sigma_C = \frac{F}{s}$$

where σ_C is the compressive strength (MPa), F is the maximum ultimate load (N), and S is the area of the specimen face under load (mm^2).

The bulk density and water absorption of the samples were determined based on Archimedes' principle, in accordance with the UNE-EN 1015-10 standard [85]. The results are presented as the average values obtained from five determinations of half specimens from each sample.

The real density of the alkaline-activated cements was measured using the pycnometer method, with ethanol as the solvent. The total porosity was then calculated using the real density and bulk density values, based on the following equation:

$$\text{Total porosity}\left(\%\right) = \left(1 - \frac{\text{bulk density}}{\text{true density}}\right) \times 1000$$

2.4. Statistical analysis

In the present study, a two-way analysis of variance (ANOVA) and an *F*-test were performed using R and R Commander to evaluate the statistical significance of the factors affecting the dependent variables, namely compressive and flexural strength. A full factorial design was implemented, and the analysis was carried out at a 95% confidence level.

3. Results and discussion

3.1. XRD analysis

The XRD spectra of the alkaline-activated cements after 28 days of curing are shown in Figure 6. The primary peaks observed in the precursor materials (Figure 3) are also present in the pastes; however, the intensity of the diffraction peaks is lower compared to the raw materials. The presence of geopolymeric gel (N–(A)–S–H) in all alkaline activation cements was confirmed with the hump between 20° and 40° [86]. In cements that incorporate AASA, BSA, and PSA with high calcium content, diffraction peaks characteristic of the formation of calcium silicate hydrate (C–S–H) are also detected, identified by the 2θ angles at 29.355°, 32.053°, and 50.077° [87]. The presence of a higher concentration of calcium (Ca) in the waste materials, coupled with the elevated pH of alkaline activator (>12) promotes the conversion of N–(A)–S–H gel into C–(A)–S–H gel [88] or hybrid gel [89].

Figure 6. Mechanical properties of alkaline-activated cements: (a) compressive strength and (b) flexural strength.

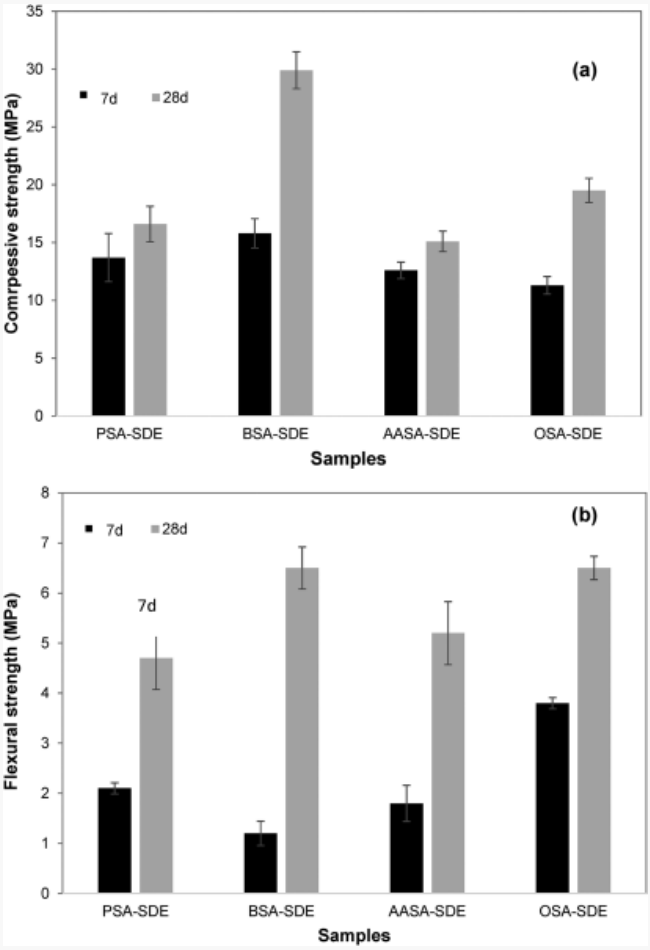

In the case of samples with PSA waste, the appearance of calcium silicate as a crystalline phase in XRD diffractogram could be overlapped with calcite, as a result of carbonation of samples in the curing process [86]. However, peaks associative to quartz have not been removed, but they were found with low intensity. In addition, in PSA-SDE diffractogram, peaks associative to larnite disappeared. The reason was that larnite can dissociate and participate in the formation of C–(A)–S–H gel, N–(A)–S–H gel or hybrid gel [90].

The anhydrite phase ($CaSO_4$) is not detected in the alkaline activation cements PSA–BSA and

AASA–BSA, due to its partial dissolution in the presence of sodium hydroxide. This condition facilitates the release of Ca^{2+} ions to the alkaline medium, which can react with silicates (SiO_4^{4-}) derived from sodium silicate, promoting the formation of hydrated calcium silicate phases (C–S–H). As the reaction progresses, by-products may be generated by the interaction of the sulfate with the alkaline solution.

The sulfate ion (SO_4^{2-}) could combine with calcium to give rise to the formation of ettringite ($3CaO{\cdot}Al_2O_3{\cdot}3CaSO_4{\cdot}32H_2O$), a new phase detected by XRD [91]. In the diffractograms of the OSA cements, the appearance of the NaH_2PO_4 phase is also observed due to the reaction of P_2O_5 and NaOH from the solution to form monosodium phosphate ($P_2O_5 + 2\ NaOH + H_2O \leftrightarrow 2\ NaH_2PO_4$). Furthermore, in the BSA-SDE samples, the peaks associated with calcite disappear, crystallizing in the form of monohydrocalcite, which, according to some authors, this phase will evolve into aragonite in longer curing periods [92].

3.2. FTIR

FTIR spectra of alkaline-activated cements after 28 days of curing are presented in Figure 7. In the FTIR spectrum of the OSA-SDE cements, a shift of the main band of the OSA residue is observed, initially centered at 1076 cm^{-1}, toward shorter wavelengths (1006 cm^{-1}), which indicates the formation of N–A–S–H geopolymeric gel. This band is attributed to the asymmetric stretching vibrations of T–O–T bonds, where T represents Si or Al atoms [93]. Other characteristic bands of N–A–S–H gels are also identified, such as the band at 545 cm^{-1}, attributed to the tetrahedral stretching of aluminum, and bands in the range of 690–420 cm^{-1}, associated with the bending vibrations of the Si bonds. –O–Si and Si–O–Al [94].

Figure 7. XRD spectrums of alkaline-activated cements at 28 days of curing: (a) PSA-SDE, (b) BSA-SDE, (c) AASA-SDE, and (d) OSA-SDE.

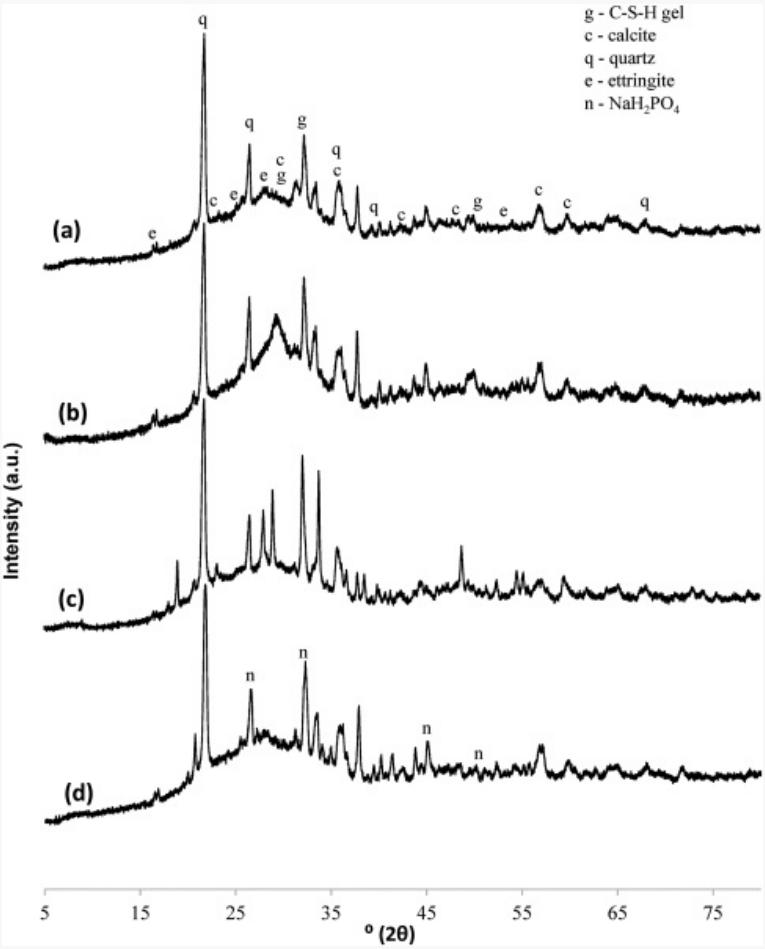

In cements that incorporate BSA, a residue with considerable amounts of calcium, the main band corresponding to the stretching vibration of the Si–O bond moves toward lower wave numbers, centered at 970 cm^{-1}, which is characteristic of the formation of C–S–H gel [95,96]. This band is wide, observing a shoulder centered at 1057 cm^{-1}, also indicating the formation of an N–A–S–H gel, suggesting the coexistence of both gels or a C, N–(A)–S–H hybrid gel. Meanwhile, the Si–O–Si bending band of the CSH gel is located at 670 cm^{-1} [97].

Concerning cements that incorporate PSA and AASA and contain considerable amounts of calcium and aluminum, the main band is observed centered at higher wave numbers 992 and 1016 cm^{-1}, respectively. These bands could be related to the characteristic Si–O–Si vibration frequency of the C–A–S–H gel [93]. Higher aluminum content in the synthesized gels suffers a shift of the main band of the spectrum toward higher wavenumbers, indicating a gel richer in aluminum [97]. The formation of the N–A–S–H geopolymeric gel is corroborated by the presence of a shoulder in the SDE-PSA cements centered at 1057 cm^{-1} and a band centered at 1055 cm^{-1} in the SDE-AASA binders.

Centered bands between 3000 and 3400 and around 1600 cm^{-1} that appear in all cements are associated with O–H bonds, corresponding with hydrated products corroborating the gel formation. The deformation and bending vibrations of the O–C–O bond characteristic of carbonates were identified in the centered bands at 1440 cm^{-1} and 860 cm^{-1}, respectively [98]. These bands result from the reaction with atmospheric CO_2, leading to the carbonation.

Furthermore, in the SDE-BSA and BSE-PSA cements, this phenomenon is also due to the presence of carbonates in the BSA and PSA precursors. The intensity of these bands decreases in the following order SDE-BSA ≈ SDE-PSA > SDE-OSA > SDE-AASA. A splitting of the band centered at 1400 cm^{-1} can be observed in the alkaline activation cements with peaks centered at 1148–1436 cm^{-1} and 1410 cm^{-1}, which could indicate the interaction between the cations Ca^{2+} and Na^{+} and the carbonate ion (CO_3^{2-}). The presence of the divalent cation Ca^{2+} induces a band with a higher wave number compared to the monovalent cation Na^{+}. This splitting suggests the coexistence of $CaCO_3$ and Na_2CO_3 [99].

3.3. Scanning electron microscopy with energy dispersive X-ray spectroscopy (SEM-EDS) analysis

The SEM images of AACs after 28 days of curing are shown in Figure 8. The microstructure varies depending on the type of sludge ash incorporated. All binders exhibit pores within the matrix, along with microcracks likely associated with the transformation of amorphous gels into more ordered structures, which induce internal stresses [100]. In cements that use BSA as a precursor, which

contains 59.36% CaO, 22.41% SiO_2, and the Al_2O_3 content being very low (2.98%), a globular gel is formed as the main reaction product, hybrid (N, C–(A)–S–H (spectrum 1). These binders presented the highest compression resistance. The use of PSA and AASA precursors with high amounts of CaO (29.5% and 35.0%) and Al_2O_3 (32.3 and 21.5%), respectively, gives rise to a Ca-poor hybrid globular gel in PAS-SDE AACs (spectrum 2). In these cements, regions are also observed in which needle-shaped sodium carbonates appear (spectrum 3) intermixed with C, N–A–S–H [101].

Figure 8. FTIR spectrums of alkaline-activated cements at 28 days of curing: (a) PSA-SDE, (b) BSA-SDE, (c) AASA-SDE, and (d) OSA-SDE.

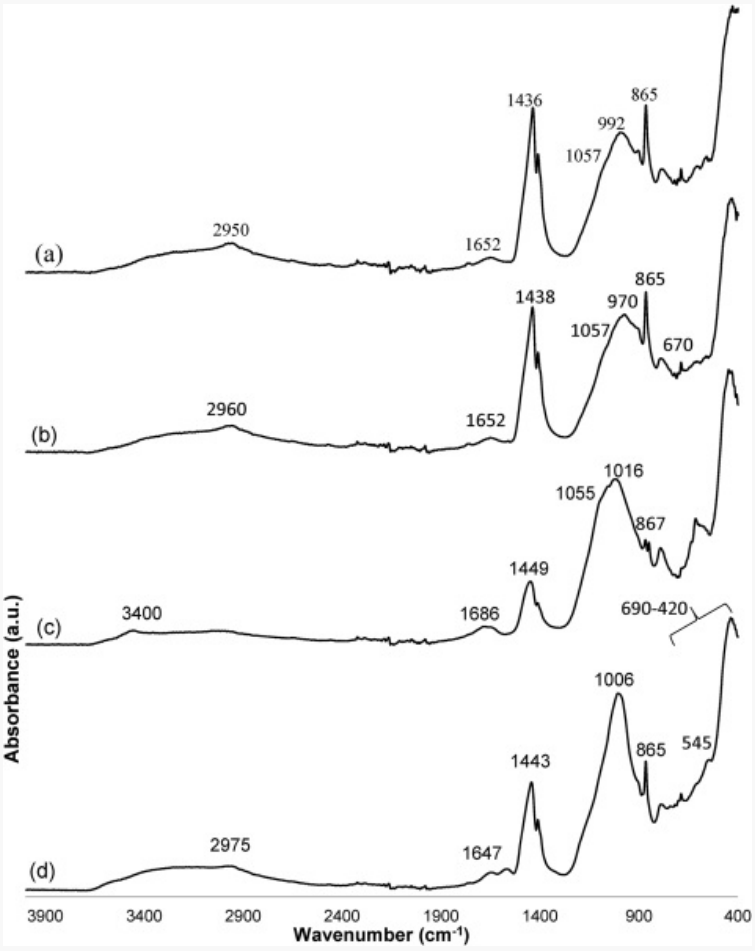

Calcium or sodium hydroxide is highly unstable and reacts easily with carbon dioxide present in the air, forming calcium and/or sodium carbonate in a carbonation process [102]. It is widely recognized that the presence of excess calcium hydroxide or sodium hydroxide in the concrete structure, combined with the subsequent carbonation process, is one of the primary factors contributing to its deterioration [102]. Furthermore, the appearance of microcracks due to its MgO content (8.1%), which can give rise to expansive phenomena due to the formation of brucite ($Mg(OH)_2$), can generate internal stresses [103]. The Ca depletion observed in the hybrid gel of PSA-BSE cements can be attributed to the reaction of Ca with P_2O_5 (13.2%) to form calcium phosphates, as well as with SO_3 (7.9%) to generate calcium sulfates, both compounds can precipitate in an alkaline medium, affecting the microstructure and properties of the alkaline-activated cement.

Two phases are observed in AASA binders: a more compact C,N–A–S–H hybrid gel containing a reduced amount of Na (spectrum 4) and a globular N,(C)–A–S–H gel containing a small amount of Ca (spectrum 5). In addition, some cracking has been evident, mainly due to the formation of ettringite needles, as seen in the micrograph (Figure 9). This phase is expansive, attributable to the high SO_3 content of the AASA precursor [104].

Figure 9. SEM images of alkaline-activated cements at 28 days of curing: (a) OS-SDE, (b) AS-SDE, (c) BS-SDE, and (d) PS-SDE.

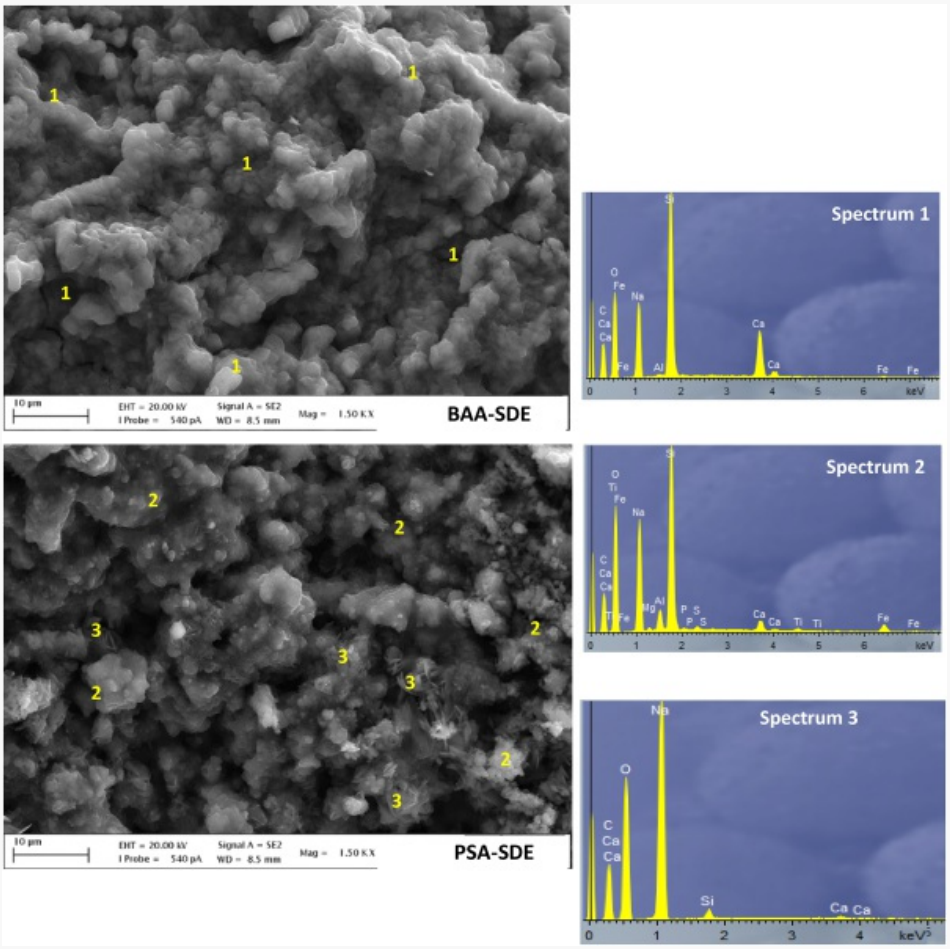

While in the cements that use OSA as a precursor containing 62.04% Al_2O_3, the main reaction product is the N–A–S–H geopolymer gel (spectrum 6). However, unreacted SDE particles (spectrum 7) and carbonates of sodium in the form of needles are also observed (spectrum 8).

3.4. Physical properties of alkaline-activated cements

The bulk density, water absorption, and total porosity of AACs measured after 7 and 28 days of curing are shown in Table 3.

Note: The table layout displayed in 'Edit' view is not how it will appear in the printed/pdf version. This html display is to enable content corrections to the table. To preview the printed/pdf presentation of the table, please view the 'PDF' tab.

Table 3. Bulk density, water absorption, and total porosity as function of curing time for alkaline-activated cements after 7 and 28 days of curing.

Physical property	Curing time	PSA-SDE	BSA-SDE	AASA-SDE	OSA-SDE
Bulk density (kg/m3)	7	1357 ± 28	1381 ± 21	1463 ± 23	1373 ± 23
	28	1560 ± 16	1729 ± 12	1547 ± 42	1500 ± 33
Water absorption (%)	7	15.31 ± 0.64	4.09 ± 0.95	5.86 ± 0.30	3.76 ± 0.62
	28	6.01 ± 0.46	0.81 ± 0.02	4.62 ± 0.17	3.66 ± 0.47
Total porosity (%)	7	35.8 ± 0.57	34.7 ± 1.23	28.6 ± 0.50	29.1 ± 0.78
	28	25.9 ± 0.59	19.6 ± 0.03	27.4 ± 0.29	24.3 ± 0.77

Place the cursor position on table column and click 'Add New' to add table footnote.

The bulk density values after 28 days of curing vary from 1500 kg/cm^3 to 1729 kg/cm^3, following the order: OSA-SDE < AASA-SDE > PSA-SDE > BSA-SDE. The actual densities of the precursors are: 2350 kg/m^3 for SDE, 2983 kg/m^3 for PSA, 2805 kg/m^3 for AASA, 2691 kg/m^3 for BSA, and 2566 kg/m^3 for OSA. Therefore, there is no relationship between the real density of the precursors and the AACs, indicating that denser reaction products are formed when BSA is used as a precursor. In this research, the *l*/*s* ratio changes depending on the sludge ash incorporated to achieve the same workability.

The greater amount of water used for OSA-SDE and AASA-SDE cements may not be consumed during the hydration process, resulting in greater internal porosity within the structure. The water absorption and total porosity values, as expected, present an inverse trend to the apparent density data; AACs with lower apparent density present greater water absorption and total porosity and vice versa. PSA and AASA present the highest water absorption values, possibly due to their high SO_3

content. This gives rise to the formation of expansive products such as ettringite according to the XRD and SEM image data.

There is a great difference between water absorption and total porosity in all binders, indicating that most of the porosity formed is closed. The formation of more compact and dense structures occurs due to the pozzolanic activity of the active silica in the SDE in the presence of Ca^{2+} cations. This activity promotes the formation of calcium aluminosilicate hydrate phases within the geopolymeric binder, acting as a microaggregate filling the spaces and pores of the conglomerate. In AASA cements, where two separate phases are formed, the porosity obtained is slightly greater.

3.5. Mechanical properties of alkali-activated cements

Compressive and flexural strength represent the most critical mechanical properties for structural building materials, as they determine the material's ability to withstand applied loads and resist deformation under stress. Mechanical results as a function of curing time for the AACs after 7 and 28 days of curing are shown in Figure 9. The compressive strength follows the order: BSA-SDE ≫ OSA-SDE > PSA-SDE ≈ AASA-SDE, and the flexural strength BSA-SDE ≈ OSA-SDE > PSA-SDE ≈ AASA-SDE. The mechanical strength of alkali-activated materials is influenced by the chemical reaction between the precursor and the alkaline activator, as well as the curing process [105].

In all cements, an increase in compressive strength is observed over time, indicating an advance in alkali-activation reactions. BSA-SDE cement presents the highest compressive and flexural strength with 30.0 and 6.5 MPa after 28 days of curing, respectively. In this system, where SDE (rich in silica) and BSA (rich in CaO and SiO_2) are combined, analysis by SEM reveals that the gel formed is globular mixed, N,C–(A)–S–H (Figure 9). OSA-SDE have lower compression and flexural strength than BSA-SDE cements, with values of 19.5 and 6.5 MPa, respectively, after 28 days of curing.

In binders where OSA (rich in Al_2O_3) is used, the main reaction product is the N–A–S–H geopolymeric gel. PSA-SDE and AASA-SDE binders have slightly lower values of both compressive and flexural strength, 16.6 and 15.1 MPa and 4.7 and 5.2 MPa, respectively. PAS and

AASA are rich in Al_2O_3 and CaO, the main reaction product in PAS cements being a mixed N,C–A–S–H gel, while in AASA cements, a more compact C,N–A–S–H gel is formed together with a globular N,C–A–S–H gel.

According to other authors [11,12,106], the presence of calcium in the precursors positively influences the compressive strength of geopolymeric matrices. The primary function of the BSA precursor is to supply dissolved calcium species, whereas PSA and AASA, in addition to calcium, contribute aluminum species that react with the silicate to form various types of calcium silicate hydrates, as well as calcium and aluminum hydrates. In BSA-SDE and PSA-SDA cements, the simultaneous formation of both geopolymer gel and C–S–H gel enhances the bonding between the various hydrated phases and unreacted particles, leading to a denser and more homogeneous matrix. The development of C–S–H gel within a geopolymeric binder may function as a microaggregate, thereby contributing to the improvement of the compressive strength of the binders [104].

In contrast, in AASA-SDE cements, the formation of geopolymer gel and C–S–H gel competes with one another. As a result, rather than one phase serving as a microaggregate to fill the gaps and voids within the binder, both reactions vie for available soluble silicates and the space necessary for their growth. Consequently, the resulting binder exhibits a disordered structure with two phases of similar size, as observed in the SEM images (Figure 9), and more residual voids will be produced, resulting in a reduction in strength [104]. Furthermore, the lower resistance achieved in the PSA-SDE, AASA-SDE, and OSA-SDE cements may be due to their high SO_3 and P_2O_5 content (Table 1).

The presence of corrosion-inhibiting phosphate ions [107] hinders the total dissolution of SiO_2 from the SDE [108], leading to lower reactivity. Furthermore, P_2O_5 can react with NaOH, forming monosodium phosphate, NaH_2PO_4 identified by XRD ($P_2O_5 + 2\ NaOH + H_2O \leftrightarrow 2\ NaH_2PO_4$), which reduces the soluble Si atoms of the sodium silicate, producing less dissolution of the SDE precursor. Thus, the OSA-SDE and PSA-SDE binders with P_2O_5 contents of 18.1% and 13.2% present lower values of mechanical resistance to compression.

The presence of SO_3 can also affect the geopolymerization process by interacting with the alkaline activators and calcium of the precursor [109]. SO_3 can contribute to the formation of expansive phases such as ettringite when combined with calcium-rich precursors. This can negatively affect the mechanical properties by causing volumetric instability and the appearance of cracks in the matrix [110]. The AASA-BSE and PAS-BSE cements have a SO_3 content of 32.9% and 7.9%, respectively, and the formation of ettringite according to the XRD analysis (Figure 7) justifies their lower compression resistance.

On the other hand, the lower compressive strength of OSA-SDE pastes can also be explained by the fact that they present a higher *l*/*b* ratio to improve workability due to their higher LOI (Table 1). The use of a greater amount of liquid results in lower compressive strength [111]. The compressive strength of AACs can present variable results since they depend on the processing conditions and the raw material used.

In a study carried out, geopolymers were synthesized using bottom ash and paper sludge ash activated with a solution of NaOH (5, 10, and 15 M) and sodium silicate (Na_2SiO_3). The optimal compressive strength results of 15 MPa were obtained when 33.33% of paper sludge ash was incorporated, and a concentration of NaOH = 15 M was used after 28 days of curing [112]. Another study investigated the use of RHA and AAS as aluminosilicate sources for the synthesis of geopolymers, using a mixture of sodium silicate and sodium hydroxide as the alkaline solution. The materials were cured at 40 °C for 28 days. The compressive strength estimated from the tensile strength indicates values of 17–39.8 MPa, obtaining the maximum when the alumina content increases with respect to silica, this is likely attributed to the influence of alumina on the degree of polymerization, rather than a mere filling effect [113]. Aluminum waste (10–60 wt.%) and fly ash were activated with a solution of (Na_2SiO_3) and sodium hydroxide (NaOH) (5.10 and 15 M) at a fixed ratio of 2.5 for geopolymerization. The geopolymers cured at room temperature reach optimal flexural and compressive strengths of 3.7 and 28.0 MPa when 40% of aluminum residue and a concentration of 10 M NaOH are incorporated, increasing the mechanical strength when curing is carried out at a temperature of 60 and 80 °C [67].

Other researchers explored the use of ashes derived from the calcination of industrial sludge from the oil refining industry (ORSA) (5–20 wt.%) in AACs based on RHA or chamotte (CHM). These cements were activated with a sustainable alternative activator solution composed of NaOH (10 M) and diatomaceous earth. Optimal flexural and compressive strength values were achieved with the incorporation of 20% ORSA, resulting in flexural strength values of 8.9 and 12.9 MPa, and compressive strength values of 15.7 and 30.6 MPa for cements based on CHM and RHA, respectively, after 28 days of curing [53]. When both RHA and CHM precursors were used with the commercial solution of sodium silicate and sodium hydroxide to mixtures incorporating 20% of ORSA very low values of flexural strength (>2 MPa) and compression (>6 MPa) were obtained due to the rapid hardening of the mixture, which prevents proper compaction. The suitability of using BSA residue as an alternative base material in geopolymeric concrete activated with an alkaline solution of NaOH and Na_2SiO_2 was also studied, obtaining compressive strengths of less than 1 MPa after 28 days of curing, indicating a weak polymerization reactivity under the processing parameters used [41].

Although the compressive strength values obtained for the AACs (ranging from 15.1 to 30.0 MPa at 28 days) are lower than those of typical structural Portland cement mortars (often between 32.5 and 52.5 MPa) after 28 days of curing under standard conditions [114], they fall within the range of non-structural or low-strength concretes used in various construction applications, such as masonry blocks, pavements, or sub-base materials. Moreover, the BSA-SDE binder reached 30 MPa after 28 days, which is comparable to Portland cement mortars with a 28-day strength class of 32.5 N. Therefore, the formulated AACs, especially those incorporating BSA, show promising performance for applications where moderate mechanical requirements are acceptable, with the additional benefit of using industrial waste as precursors.

3.6. Statistical analysis: multi-way ANOVA test

In order to assess their impact on compressive and flexural strength, two factors were carefully examined: the type of sample and the duration of curing. Table 4 provides a comprehensive overview of the experimental results, detailing the factors under investigation and the specific levels at which each factor was evaluated.

Note: The table layout displayed in 'Edit' view is not how it will appear in the printed/pdf version. This html display is to enable content corrections to the table. To preview the printed/pdf presentation of the table, please view the 'PDF' tab.

Table 4. Results of ANOVA for compressive and flexural strength.

Factor	Sum Sq	df	*F* Value	Pr(>*F*)	Significance
ANOVA for compressive strength					
Curing time	522.87	1	537.148	<2.2e − 16	Significant
Sample	467.96	3	160.244	<2.2e − 16	Significant
Curing time; sample	194.40	3	66.568	7.547e − 14	Significant
Residuals	31.15	32			
ANOVA for flexural strength					
Curing time	135.719	1	591.976	<2.2e − 16	Significant
Sample	32.697	3	47.539	6.797e − 12	Significant
Curing time; sample	9.580	3	13.929	5.562e − 06	Significant
Residuals	7.336	32			

Sum Sq: measure of variation or deviation from the mean calculated as a summation of the squares of the differences from the mean; df: degrees of freedom of the *F* statistic; *F* value: value on the *F* distribution calculated by dividing two mean squares; Pr(>*F*): *p* Value associated with the *F* statistic for each individual factor and the interactions between them; significance: measure of reliability in the results of the analysis; residuals: difference between the observed value of the dependent variable and the predicted value.

Consistent with the aforementioned analysis, *p* values of significance were found to be ≪0.05, leading to the rejection of the null hypothesis. It was concluded that both factors – sample type and curing time – as well as their interaction, had a significant effect on the compressive and flexural strength outcomes. The high *F*-value further indicated substantial variation in the parameters, highlighting their strong influence on the results.

4. Conclusions

The study compares the physical, mechanical and microstructural properties of AACs based on SDE from the brewing industry (SDE) in which 20 wt.% of sludge ashes from different industrial activities has been incorporated individually: PSA, BSA, AASA, and OSA. The main conclusions drawn from the study are:

- The chemical composition of the ashes significantly influences the gel phases formed and, therefore, the physical and mechanical properties of the AACs. The SDE residue, rich in silica, together with the incorporation of OSA (rich in aluminum), gives rise to the formation of geopolymeric gel (N–A–S–H). In the case of BSA-SDE, PSA-SDE, and AASA-SDE cements, the incorporation of BSA (rich in calcium) and the incorporation of PSA and AASA (both rich in calcium and alumina), promote the formation of N,C–(A)–S–H hybrid gels. However, in AASA-SDE cement, two separate hybrid gels are observed, one richer in calcium C,N–A–S–H and another richer in sodium N–A–S–H, which partly justifies its lower mechanical resistance.
- An optimal compressive strength of 30 MPa is obtained for BSA-SDE cements. In contrast, the lower resistance obtained for cements that incorporate OSA, PSA, and AASA could be due to the high contents of P_2O_5 and/or SO_3 present in their composition, which can induce the formation of expansive products or secondary reaction products that inhibit dissolution of the precursor, negatively affecting the mechanical properties.
- XRD and FTIR analysis confirmed the presence of geopolymeric gels in all AACs, and (C–S–H) or (C–S–A–H) gel in the case of calcium-rich or calcium–aluminum-rich cements, respectively.
- Two-way ANOVA and *F*-test carried out statistically confirm what was already assumed, the significance of the curing time and the raw material used and their interaction on the resulting technological properties of the materials obtained.

Although based on the above, the feasibility of using different ashes from industrial sewage sludge as a by-product for the manufacture of BDS-based CSA is demonstrated, some limitations need to be acknowledged. It is crucial to control the chemical composition of the precursors, minimizing the content of SO_3, P_2O_5, and Mn_2O since they promote the formation of expansive products or the partial consumption of silica and calcium for the formation of secondary products that negatively influence the mechanical properties of the AACs. Therefore, the variability in the composition of these wastes from different sources may affect the reproducibility and generality of the results or scalability. The availability of these wastes is geographically limited, as they are generated by specific industrial sectors. On the other hand, the study focused mainly on short-term (7 and

28 days) mechanical and microstructural characterization, without assessing long-term mechanical and durability properties under various environmental conditions, including resistance to chemical exposure or freeze–thaw cycles. In addition, potential environmental impacts related to heavy metal leaching from AACs, which should be addressed to ensure the environmental safety of the applications, were not examined. Depending on the mechanical properties obtained, they could be used for various construction applications, in particular for prefabricated elements such as paving units, blocks and load-bearing and non-structural components. Future work will address these aspects to further validate the performance and applicability of the proposed materials.

Acknowledgements

The authors thank Heineken S. L. companies for supplying the brewery sludge and the diatomaceous earth; Aceites del Sur Coosur, S.A. for the oil sludge; Cotton South S.L. Celsur for the pulp–paper sludge; and Alusistemas S.A. for the aluminum anodization sludge. Technical and human support provided by CICT of Universidad de Jaén (UJA, MINECO, Junta de Andalucía, FEDER) is gratefully acknowledged.

Disclosure statement

No potential conflict of interest was reported by the author(s).

Data availability statement

The data that support the findings of this study are openly available in Zenodo at http://doi.org.10.5281/zenodo.15308523

Note: this Edit/html view does not display references as per your journal style. There is no need to correct this. The content is correct and it will be converted to your journal style in the published version.

References

1 Benhelal E, Shamsaei E, Rashid MI. Challenges against CO_2 abatement strategies in cement industry: a review. J Environ Sci. 2021;104:84–101. doi: 10.1016/j.jes.2020.11.020.

2 Benhelal E, Zahedi G, Hashim H. A novel design for green and economical cement manufacturing. J Clean Prod. 2012;22(1):60–66. doi: 10.1016/j.jclepro.2011.09.019.

3 Zhang P, Zheng Y, Wang K, et al. A review on properties of fresh and hardened geopolymer mortar. Compos Part B Eng. 2018;152:79–95. doi: 10.1016/j.compositesb.2018.06.031.

4 Davidovits J. Geopolymer chemistry and applications. 5th ed. Saint Quentin: Geopolymer Institute; 2020.

5 Singh N, Kumar M, Rai S. Geopolymer cement and concrete: properties. Mater Today Proc. 2020;29:743–748. doi: 10.1016/j.matpr.2020.04.513.

6 Eliche-Quesada D, Calero-Rodríguez A, Bonet-Martínez E, et al. Geopolymers made from metakaolin sources, partially replaced by Spanish clays and biomass bottom ash. J Build Eng. 2021;40:102761. doi: 10.1016/j.jobe.2021.102761.

7 Alhawat M, Ashour A, Yildirim G, et al. Properties of geopolymer sourced from construction and demolition waste: a review. J Build Eng. 2022;50:104104. doi: 10.1016/j.jobe.2022.104104.

8 Wang X, Zhang C, Zhu H, et al. Reaction kinetics and mechanical properties of a mineral-micropowder/metakaolin-based geopolymer. Ceram Int. 2022;48:14173–14181. doi: 10.1016/j.jobe.2022.104104.

9 Lazorenko G, Kasprzhitskii A, Fini EH. Sustainable construction via novel geopolymer composites incorporating waste plastic of different sizes and shapes. Constr Build Mater. 2022;324:126697. doi: 10.1016/j.conbuildmat.2022.126697.

10 Sharma A, Singh P, Kapoor K. Utilization of recycled fine powder as an activator in fly ash-based geopolymer mortar. Constr Build Mater. 2022;323:126581. doi: 10.1016/j.conbuildmat.2022.126581.

11 Zawrah M, Sadek H, Ngida REA, et al. Effect of low-rate firing on physico-mechanical properties of unfoamed and foamed geopolymers prepared from waste clays. Ceram Int. 2022;48(8):11330–11337. doi: 10.1016/j.ceramint.2021.12.356.

12 Liang G, Zhu H, Li H, et al. Comparative study on the effects of rice husk ash and silica fume on the freezing resistance of metakaolin-based geopolymer. Constr Build Mater. 2021;293:123486. doi: 10.1016/j.conbuildmat.2021.123486.

13 Li Y, Chen D, Yu K, et al. Mix design and performance of low-carbon alkali-activated slag/bagasse ash cementitious materials. J Build Eng. 2024;90:109468. doi: 10.1016/j.jobe.2024.109468.

14 Du Y, Pundienė I, Pranckevičienė J, et al. A review of biomass wood ash in alkali-activated materials: treatment, application, and outlook. J Compos Sci. 2024;8(5):161. doi: 10.3390/jcs8050161.

15 Zhang B, Peng H, Xiong T, et al. Towards enhancing the durability of seawater coral aggregate concrete under drying-wetting cycles with slag-based geopolymers. J Sustain Cem Based Mater. 2024;13(3):389–401. doi: 10.1080/21650373.2023.2278846.

16 Kandalai S, Patel A. Alkali activation of red mud and GGBS blends for expansive soil stabilization: strength, durability and leachate studies. Indian Geotech J. 2025. doi: 10.1007/s40098-025-01183-w.

17 Murmu AL, Jain A, Patel A. Mechanical properties of alkali activated fly ash geopolymer stabilized expansive clay. KSCE J Civ Eng. 2019;23(9):3875–3888. doi: 10.1007/s12205-019-2251-z.

18 Murmu AL, Patel A. Studies on the properties of fly ash|rice husk ash based geopolymer for use in black cotton soils. Int J Geosynth Ground Eng. 2020;6:38. doi: 10.1007/s40891-020-00224-z.

19 Murmu AL, Dhole N, Patel A. Stabilisation of black cotton soil for subgrade application using fly ash geopolymer. Road Mater Pavement Des. 2020;21(3):867–885. doi: 10.1080/14680629.2018.1530131.

20 Ferraz E, Coroado J, Silva J, et al. Manufacture of ceramic bricks using recycled brewing spent kieselguhr. Mater Manuf Process. 2011;26(10):1319–1329. doi: 10.1080/10426914.2011.551908.

21 Gómez J, Gil M, de la Rosa-Fox N, et al. Diatomite releases silica during spirit filtration. Food Chem. 2014;159:381–387. doi: 10.1016/j.foodchem.2014.02.157.

22 Yılmaz B, Ediz N. The use of raw and calcined diatomite in cement production. Cem Concr Compos. 2008;30(3):202–211. doi: 10.1016/j.cemconcomp.2007.08.003.

23 Gong X, Tian W, Wang L, et al. Biological regeneration of brewery spent diatomite and its reuse in basic dye and chromium (III) ions removal. Process Saf Environ Prot. 2019;128:353–361. doi: 10.1016/j.psep.2019.05.024.

24 Zhang H, He B, Zhao B, et al. Using diatomite as a partial replacement of cement for improving the performance of recycled aggregate concrete (RAC)—effects and mechanism. Constr Build Mater. 2023;385:131518. doi: 10.1016/j.conbuildmat.2023.131518.

25 Letelier V, Tarela E, Muñoz P, et al. Assessment of the mechanical properties of a concrete made by reusing both: brewery spent diatomite and recycled aggregates. Constr Build Mater. 2016;114:492–498. doi: 10.1016/j.conbuildmat.2016.03.177.

26 Lv H, Jiang A, Jin J. Influence of ultrafine diatomite on cracking behavior of concrete: an acoustic emission analysis. Constr Build Mater. 2021;308:124993. doi: 10.1016/j.conbuildmat.2021.124993.

27 Galán-Arboledas R, Cotes-Palomino M, Bueno S, et al. Evaluation of spent diatomite incorporation in clay-based materials for lightweight bricks processing. Constr Build Mater. 2017;144:327–337. doi: 10.1016/j.conbuildmat.2017.03.202.

28 Tanniratt P, Wasanapiarnpong T, Mongkolkachit C, et al. Utilization of industrial wastes for preparation of high performance ZnO/diatomite hybrid photocatalyst. Ceram Int. 2016;42(15):17605–17609. doi: 10.1016/j.ceramint.2016.08.074.

29 Yitbarek M, Abdeta K, Beyene A, et al. Experimental evaluation of sorptive removal of fluoride from drinking water using natural and brewery waste diatomite. Process Saf Environ Prot.

2019;128:95–106. doi: 10.1016/j.psep.2019.05.052.

30 Gong X, Tian W, Bai J, et al. Highly efficient deproteinization with an ammonifying bacteria *Lysinibacillus fusiformis* isolated from brewery spent diatomite. J Biosci Bioeng. 2019;127(3):326–332. doi: 10.1016/j.jbiosc.2018.08.004.

31 Dessalew G, Beyene A, Nebiyu A, et al. Effect of brewery spent diatomite sludge on trace metal availability in soil and uptake by wheat crop, and trace metal risk on human health through the consumption of wheat grain. Heliyon. 2018;4(9):e00967. doi: 10.1016/j.heliyon.2018.e00783.

32 Cheng X, Zhang H, Li W, et al. Utilizing diatomaceous earth (DE) as a sustainable substitute in alkali-activated cementitious materials: performance and life cycle assessment. Constr Build Mater. 2024;452:138889. doi: 10.1016/j.conbuildmat.2024.138889.

33 García-Díaz A, Bueno-Rodríguez S, Felipe-Sesé MA, et al. Effect of the incorporation of spent diatomaceous earths on the properties of alkaline activation cements based on sewage sludge ash. Archiv Civ Mech Eng. 2024;24(2):62. doi: 10.1007/s43452-024-00873-1.

34 Ministerio de Medio Ambiente y Medio Rural y Marino. El medio ambiente y el medio rural y marino en españa 2009. Madrid: Secretaría General Técnica; 2009.

35 Instituto Nacional de Estadística. Producción de lodos en España; 2022. AQ3

36 Fillaudeau L, Blanpain-Avet P, Daufin G. Water, wastewater and waste management in brewing industries. J Clean Prod. 2006;14(5):463–471. doi: 10.1016/j.jclepro.2005.01.002.

37 Assefa F, Gebremedhin Z, Alem T. Data on the effects of brewery sludge and blended NPS fertilizer rates on yield and yield components of maize (*Zea mays* L.) in North Mecha district, northwestern Ethiopia. Data Brief. 2023;51:109707. doi: 10.1016/j.dib.2023.109707.

38 Alemu N, Ahmed A, Mohammed M. Impact of brewery waste sludge on sorghum (*Sorghum bicolor* L. Moench) productivity and soil fertility in Harari Regional State, Eastern Ethiopia. Turk J Agric Food Sci Technol. 2017;5:366–372. doi: 10.24925/turjaf.v5i4.366-372.1058.

39 Tsadik YKG, Hailu AM, Asfaw SL, et al. The effect of brewery sludge biochar on immobilization of bio-available cadmium and growth of *Brassica carinata*. Heliyon. 2020;6(12):e05614. doi: 10.1016/j.heliyon.2020.e05573.

40 Gemeda TN, Melaku YT, Chamada TA, et al. Optimization mixing ratio of the brewery wastewater sludge and coal as energy source for cement industry and fuel ash effect on the raw material composition. Environ Challenges. 2022;7:100476. doi: 10.1016/j.envc.2022.100476.

41 Okeyinka OM, Oloke DA, Adebisi WA, et al. Investigation into the applicability of brewery sludge residue-ash as a base material for geopolymer concrete. Constr Build Mater. 2019;223:28–32. doi: 10.1016/j.conbuildmat.2019.06.214.

42 Farías RD, Martínez C, Cotes T, et al. Effects of wastes from the brewing industry in lightweight aggregates manufactured with clay for green roofs. Materials. 2017;10(5):527. doi: 10.3390/ma10050527.

43 Taylor RP, Jones CL, Laubscher RK. Empirical comparison of activated sludge and high rate algal ponding technologies used to recover water, nitrogen and carbon from brewery effluent. J Water Process Eng. 2021;40:101840. doi: 10.1016/j.jwpe.2020.101840.

44 Taylor RP, Jones CL, Laubscher RK. Recovery of methane and adding value to the digestate of biomass produced by high rate algal ponds or waste activated sludge, used to treat brewery effluent. J Water Process Eng. 2021;40:101797. doi: 10.1016/j.jwpe.2020.101797.

45 Doula MK, Moreno-Ortego JL, Tinivella F, et al. Olive mill waste: recent advances for the sustainable development of olive oil industry. In: Olive mill waste: recent advances for sustainable management. Academic Press; 2017. p. 29–56.AQ4

46 Gómez S, Fernández-Rodríguez D, Peña D, et al. Olive mill sludge may reduce water contamination by 4-chloro-2-methylphenoxyacetic acid (MCPA) in non-flooding but enhance it in flooding rice cropping agroecosystems. Sci Total Environ. 2020;707:136000. doi: 10.1016/j.scitotenv.2019.136000.

47 Kypritidou Z, El-Bassi L, Jellali S, et al. Lead removal from aqueous solutions by olive mill wastes derived biochar: batch experiments and geochemical modelling. J Environ Manage. 2022;318:115562. doi: 10.1016/j.jenvman.2022.115562.

48 Roccamante M, Ruiz-Delgado A, Cabrera-Reina A, et al. Microcontaminant removal in solar pilot scale photoreactors with commercial iron nanoparticles obtained from olive mill wastewater. Catal Today. 2023;413–415:113968. doi: 10.1016/j.cattod.2022.11.029.

49 Messineo A, Picciotto Maniscalco M, Volpe R. Biomethane recovery from olive mill residues through anaerobic digestion: a review of the state of the art technology. Sci Total Environ. 2020;703:135508. doi: 10.1016/j.scitotenv.2019.135508.

50 de la Casa JA, Bueno JS, Castro E. Recycling of residues from the olive cultivation and olive oil production process for manufacturing of ceramic materials. A comprehensive review. J Clean Prod. 2021;296:126436. doi: 10.1016/j.jclepro.2021.126436.

51 Eliche-Quesada D, Azevedo-Da Cunha R, Corpas-Iglesias F. Effect of sludge from oil refining industry or sludge from pomace oil extraction industry addition to clay ceramics. Appl Clay Sci. 2015;114:202–211. doi: 10.1016/j.clay.2015.06.009.

52 Mekki H, Anderson M, Benzina M, et al. Valorisation of olive mill wastewater by its incorporation in building bricks. J Hazard Mater. 2008;158(2–3):308–315. doi: 10.1016/j.jhazmat.2008.02.024.

53 Garcia-Diaz A, Bueno-Rodríguez S, Pérez-Villarejo L, et al. Reuse of oil refining sludge residue ash via alkaline activation in matrices of chamotte or rice husk ash. Mater. 2023;16(7):2801. doi: 10.3390/ma16071072.

54 Toczyłowska-Mamińska R. Limits and perspectives of pulp and paper industry wastewater treatment – a review. Renew Sustain Energy Rev. 2017;78:764–772. doi: 10.1016/j.rser.2017.04.053.

55 de Azevedo ARG, Alexandre J, Xavier GC, et al. Recycling paper industry effluent sludge for use in mortars: a sustainability perspective. J Clean Prod. 2018;192:335–346. doi:

10.1016/j.jclepro.2018.04.171. AQ5

56 Cavdar AD, Yel H, Boran S, et al. Cement type composite panels manufactured using paper mill sludge as filler. Constr Build Mater. 2017;142:410–416. doi: 10.1016/j.conbuildmat.2017.03.113.

57 Vieira CMF, Pinheiro RM, Rodriguez RJS. Clay bricks added with effluent sludge from paper industry: technical, economical and environmental benefits. Appl Clay Sci. 2016;132–133:753–759. doi: 10.1016/j.clay.2016.07.010.

58 Chen M, Zheng Y, Zhou X, et al. Recycling of paper sludge powder for achieving sustainable and energy-saving building materials. Constr Build Mater. 2019;229:116767. doi: 10.1016/j.conbuildmat.2019.116767.

59 Yan S, Sagoe-Crentsil K. Evaluation of fly ash geopolymer mortar incorporating calcined wastepaper sludge. J Sustain Cement Based Mater. 2016;5(6):370–380. doi: 10.1080/21650373.2016.1174962.

60 Azevedo A, Marvila T, Fernandes WJ, et al. Assessing the potential of sludge generated by the pulp and paper industry in assembling locking blocks. J Build Eng. 2019;23:334–340. doi: 10.1016/j.jobe.2019.03.013.

61 International Aluminium Institute. Primary aluminium production; 2024 [accessed 2024 Sep 28]. Available from: https://international-aluminium.org/statistics/primary-aluminium-production/

62 Mymrin V, Molinetti A, Alekseev K, et al. Characterization of construction materials on the base of mortar waste, activated by aluminium anodisation sludge and lime production waste. Constr Build Mater. 2019;212:202–209. doi: 10.1016/j.conbuildmat.2018.11.085.

63 Mymrin V, Pedroso DE, Pedroso C, et al. Environmentally clean composites with hazardous aluminium anodising sludge, concrete waste, and lime production waste. J Clean Prod. 2018;174:380–388. doi: 10.1016/j.jclepro.2018.02.156.

64 Mymrin V, Pedroso DE, Pedroso CL, et al. Physical–chemical processes of sustainable construction materials structure formation with iron ore processing tailings and aluminium anodising

sludge. Constr Build Mater. 2021;298:123698. doi: 10.1016/j.conbuildmat.2021.123698.

65 Valdevino D, Barcelos RL, Cremona GO, et al. Recycled polyethylene terephthalate and aluminium anodising sludge-based boards with flame resistance. Waste Manag. 2019;92:1–14. doi: 10.1016/j.wasman.2019.10.017.

66 Lipowska B, Kusiorowski R, Gerle A, et al. Recycling of residual sludge from aluminium anodising in fired clay bricks. Clean Waste Syst. 2022;3:100055. doi: 10.1016/j.clws.2022.100055.

67 da Silva NB, Ferreira D, Bernardin AM. Valorisation of rice husk ash and aluminium anodising sludge as precursors for the synthesis of geopolymers. J Clean Prod. 2021;298:126770. doi: 10.1016/j.jclepro.2021.126770.AQ6

68 Govindan B, Kumarasamy V. Sustainable valorisation through the reuse of incinerated paper mill sludge ash in building brick production. Constr Build Mater. 2024;439:137291. doi: 10.1016/j.conbuildmat.2024.137291.

69 Kizinievič O, Kizinievič V, Trambitski Y, et al. Lightweight composite materials made of paper sludge and corn starch. Ind Crops Prod. 2024;208:117847. doi: 10.1016/j.indcrop.2024.117847.

70 Eliche-Quesada D, Martínez-García C, Martínez-Cartas M, et al. The use of different forms of waste in the manufacture of ceramic bricks. Appl Clay Sci. 2011;52(3):270–276. doi: 10.1016/j.clay.2011.07.003.

71 Lynn C, Dhir R, Ghataora G, et al. Sewage sludge ash characteristics and potential for use in concrete. Constr Build Mater. 2015;98:767–779. doi: 10.1016/j.conbuildmat.2015.06.073.

72 Felaous K, Aziz A, Achab M. Physico-mechanical and durability properties of new eco-material based on blast furnace slag activated by Moroccan diatomite gel. Environ Sci Pollut Res Int. 2023;30(2):3549–3561. doi: 10.1007/s11356-022-22156-z.

73 Davidovits J. Geopolymers inorganic polymeric new materials. J Therm Anal.

1991;37(8):1633–1656. doi: 10.1007/BF01912193.

74 Pantazopoulou E, Zebiliadou O, Mitrakas M, et al. Stabilization of tannery sludge by co-treatment with aluminium anodising sludge and phytotoxicity of end-products. Waste Manag. 2017;61:327–336. doi: 10.1016/j.wasman.2017.01.025.

75 Zhang J, Liu B, Zhao S, et al. Preparation and characterization of glass ceramic foams based on municipal solid waste incineration ashes using secondary aluminium ash as foaming agent. Constr Build Mater. 2020;262:120781. doi: 10.1016/j.conbuildmat.2020.120781.

76 Ferone C, Liguori B, Capasso I, et al. Thermally treated clay sediments as geopolymer source material. Appl Clay Sci. 2015;107:195–204. doi: 10.1016/j.clay.2015.01.022.

77 Gómez-Casero M, Pérez-Villarejo L, Sánchez-Soto P, et al. Comparative study of alkali activated cements based on metallurgical slags, in terms of technological properties developed. Sustain Chem Pharm. 2022;29:100746. doi: 10.1016/j.scp.2022.100746.

78 Maheswaran R, Marichelvam MK, Asok SP. Development of value-added sustainable products from paper mill sludge: an experimental approach. Heliyon. 2023;9(6):e17517. doi: 10.1016/j.heliyon.2023.e17517.

79 Sun F, Chen J, Sun Z, et al. Promoting bioremediation of brewery wastewater, production of bioelectricity and microbial community shift by sludge microbial fuel cells using biochar as anode. Sci Total Environ. 2024;929:172418. doi: 10.1016/j.scitotenv.2024.172418.

80 Morsy MS, Alsayed SH, Al-Salloum Y, et al. Effect of sodium silicate to sodium hydroxide ratios on strength and microstructure of fly ash geopolymer binder. Arab J Sci Eng. 2014;39(6):4333–4339. doi: 10.1007/s13369-014-1093-8.

81 Firdous R, Stephan D. Effect of silica modulus on the geopolymerization activity of natural pozzolans. Constr Build Mater. 2019;219:31–43. doi: 10.1016/j.conbuildmat.2019.05.161.

82 Babu T, Thangaraj S. A novel approach for the synthesis of eco-friendly geopolymer ternary blended mortar with GGBS, sugarcane bagasse ash, and sewage sludge ash under ambient curing

conditions. KSCE J Civ Eng. 2023;27(8):3441–3454. doi: 10.1007/s12205-023-1842-x.

83 Kong X, Shi J, Shen Y, et al. Sludge-based geopolymer materials: a review. Int J Appl Ceram Technol. 2024;21(3):1333–1365. May;21 doi: 10.1111/ijac.14714.

84 UNE-EN 1015-11:2000/A1:2007. Test methods for mortars for masonry. Part 11: determination of the flexural and compressive strength of hardened mortar. Spanish Association for Standardisation; 2007.AQ7

85 UNE-EN 1015-10:2000. Test methods for mortars for masonry. Part 10: determination of the dry bulk density of hardened mortar. Spanish Association for Standardisation; 2000.AQ8

86 Gómez-Casero MA, Pérez-Villarejo L, Castro E, et al. Effect of steel slag and curing temperature on the improvement in technological properties of biomass bottom ash based alkali-activated materials. Constr Build Mater. 2021;302:124205. doi: 10.1016/j.conbuildmat.2021.124205.

87 Yousefi Oderji S, Chen B, Riaz Ahmad M, et al. Fresh and hardened properties of one-part fly ash-based geopolymer binders cured at room temperature: effect of slag and alkali activators. J Clean Prod. 2019;225:1–10. doi: 10.1016/j.jclepro.2019.03.290.

88 Lee WK, van Deventer JSJ. Effects of anions on the formation of aluminosilicate gel in geopolymers. Ind Eng Chem Res. 2002;41(18):4550–4558. doi: 10.1021/ie010937i.

89 Gómez-Casero M, Calado L, Romano P, et al. Acorn gasification char valorisation in the manufacture of alkali activated materials. Constr Build Mater. 2023;407:133533. doi: 10.1016/j.conbuildmat.2023.133533.

90 Shao N, Tang S, Liu Z, et al. Hierarchically structured calcium silicate hydrate-based nanocomposites derived from steel slag for highly efficient heavy metal removal from wastewater. ACS Sustain Chem Eng. 2018;6(11):14926–14935. doi: 10.1021/acssuschemeng.8b03428.

91 Shi C, Fernández-Jiménez A, Palomo A. New cements for the 21st century: the pursuit of an alternative to Portland cement. Cem Concr Res. 2011;41(7):750–763. doi:

10.1016/j.cemconres.2011.03.016.

92 González-López J, Fernández-González A, Jiménez A. Influencia del CO_2 en el polimorfismo del $CaCO_3$. Rev Soc Esp Miner. 2012;16:174–175. doi: 10.1007/s00410-012-0781-2.

93 Zhang Z, Wang H, Provis JL. Quantitative study of the reactivity of fly ash in geopolymerization by FTIR. J Sustain Cem Based Mater. 2012;1(4):154–166. doi: 10.1080/21650373.2012.752620.

94 Criado M, Fernández-Jiménez A, Palomo A. Alkali activation of fly ash: effect of the SiO_2/Na_2O ratio: part I: FTIR study. Microporous Mesoporous Mater. 2007;106(1–3):180–191. doi: 10.1016/j.micromeso.2007.03.029.

95 Yu P, Kirkpatrick R, Poe B, et al. Structure of calcium silicate hydrate (C–S–H): near-, mid-, and far-infrared spectroscopy. J Am Ceram Soc. 1999;82:742–748. doi: 10.1111/j.1151-2916.1999.tb01826.x.

96 Fernández-Jiménez A, Palomo A. Alkali activated fly ashes. Structural studies through mid-infrared spectroscopy. Microporous Mesoporous Mater. 2005;86:207–214. doi: 10.1016/j.micromeso.2005.05.057.

97 García-Lodeiro I, Fernández-Jiménez A, Blanco-Varela M, et al. Synthesis and characterization of cementitious gels (C–S–H and N–A–S–H) compatibility studies. In: Proceedings of the 13th International Congress on the Chemistry of Cement; Madrid; 2011.AQ9

98 Lee WKW, van Deventer JSJ. Use of infrared spectroscopy to study geopolymerization of heterogeneous amorphous aluminosilicates. Langmuir. 2003;19(21):8726–8734. doi: 10.1021/la026127e.

99 Fine G, Stolper E. Dissolved carbon dioxide in basaltic glasses: concentrations and speciation. Earth Planet Sci Lett. 1986;76(3–4):263–278. doi: 10.1016/0012-821X(86)90077-3.

100 Luukkonen T, Abdollahnejad Z, Yliniemi J, et al. One-part alkali-activated materials: a review. Cem Concr Res. 2018;103:21–34. doi: 10.1016/j.cemconres.2017.10.004.

101 Burciaga-Díaz O, Escalante-García J. Structural transition to well-ordered phases of NaOH-activated slag-metakaolin cements aged by 6 years. Cem Concr Res. 2022;156:106791. doi: 10.1016/j.cemconres.2022.106791.

102 Glukhovsky VD. Ancient, modern and future concretes In: Proceedings of the 1st International Conference on Alkaline Cements and Concretes; Kiev, Ukraine; 1994. p. 53–62. AQ10

103 Shi C. Characteristics and cementitious properties of ladle slag fines from steel production. Cem Concr Res. 2002;32(3):459–462. doi: 10.1016/S0008-8846(01)00707-4.

104 Yip CK, Lukey GC, van Deventer JSJ. The coexistence of geopolymeric gel and calcium silicate hydrate at the early stage of alkaline activation. Cem Concr Res. 2005;35(9):1688–1697. doi: 10.1016/j.cemconres.2005.01.004.

105 Zhang M, El-Korchi T, Zhang G, et al. Synthesis factors affecting mechanical properties, microstructure, and chemical composition of red mud–fly ash based geopolymers. Fuel. 2014;134:315–325. doi: 10.1016/j.fuel.2014.05.058.

106 Nadziri N, Ismail I, Hamdan S. Binding gel characterization of alkali-activated binders based on palm oil fuel ash (POFA) and fly ash. J Sustain Cem Based Mater. 2018;7(1):1–14. doi: 10.1080/21650373.2017.1299054.

107 Yohai L, Vázquez M, Valcarce M. Phosphate ions as corrosion inhibitors for reinforcement steel in chloride-rich environments. Electrochim Acta. 2013;102:88–96. doi: 10.1016/j.electacta.2013.04.029.

108 Tchakouté H, Rüscher C, Kong S, et al. Comparison of metakaolin-based geopolymer cements from commercial sodium waterglass and sodium waterglass from rice husk ash. J Sol–Gel Sci Technol. 2016;78(3):492–506. doi: 10.1007/s10971-016-4132-0.

109 Kaladharan G, Rajabipour F. Evaluation and beneficiation of high sulfur and high alkali fly ashes for use as supplementary cementitious materials in concrete. Constr Build Mater. 2022;339:127672. doi: 10.1016/j.conbuildmat.2022.127672.

110 Antiohos SK, Papageorgiou D, Chaniotakis E, et al. Mechanical and durability characteristics of gypsum-free blended cements incorporating sulphate-rich reject fly ash. Cem Concr Compos. 2007;29(7):550–558. doi: 10.1016/j.cemconcomp.2007.03.001.

111 Abdollahnejad Z, Hlavacek P, Miraldo S, et al. Compressive strength, microstructure and hydration products of hybrid alkaline cements. Mater Res. 2014;17(4):829–837. doi: 10.1590/S1516-14392014005000056.

112 Antunes Boca Santa RA, Bernardin A, Gracher Riella H, et al. Geopolymer synthetized from bottom coal ash and calcined paper sludge. J Clean Prod. 2013;57:302–307. doi: 10.1016/j.jclepro.2013.06.029.

113 Onutai S, Jiemsirilers S, Thavorniti P, et al. Aluminium hydroxide waste based geopolymer composed of fly ash for sustainable cement materials. Constr Build Mater. 2015;101:298–308. doi: 10.1016/j.conbuildmat.2015.10.029.

114 EN 197-1:2011. Cement – part 1: composition, specifications and conformity criteria for common cements. European Committee for Standardization; 2011.AQ11

Author Query

1. **Query** [AQ0] : Please review the table of contributors below and confirm that the first and last names are structured correctly and that the authors are listed in the correct order of contribution. This check is to ensure that your names will appear correctly online and when the article is indexed.

Sequence	Prefix	Given name(s)	Surname	Suffix
1		M.	Felipe-Sesé	
2		A.	García-Díaz	
3		M. A.	Gómez-Casero	
4		D.	Eliche-Quesada	

Response by Author: "Accepted"

2. **Query** [AQ1] : Please confirm the author names as set in the proof are accurate.
Response by Author: "Accepted"

3. **Query** [AQ2] : Figure 5 was not cited in the text so a citation has been inserted. Please provide a correction if this is inaccurate.
Response by Author: "Answered within text"

4. **Query** [AQ3] : Please provide the missing city for the [35] references list entry.
Response by Author: "Spain"

5. **Query** [AQ4] : Please provide missing Editor names and city for the [45] references list entry.
Response by Author: "Doula MK, Moreno-Ortego JL, Tinivella F, Inglezakis VJ, Sarris A, Komnitsas K. Olive mill waste: Recent advances for the sustainable

development of olive oil industry. In: ICharis M. Galanakis editor. Olive Mill Waste: Recent Advances for Sustainable Management. London: Academic Press; 2017. p. 29–56. Preguntar a ChatGPT "

6. **Query** [AQ5] : References [55 and 61] are duplicate references. Hence Ref. [61] has been deleted and subsequent references have been renumbered. Please check.
Response by Author: "Accepted"

7. **Query** [AQ6] : References [68, 75 and 115] are duplicate references. Hence Refs. [75 and 115] have been deleted and subsequent references have been renumbered. Please check.
Response by Author: "Accepted"

8. **Query** [AQ7] : Please provide missing city for the [84] references list entry.
Response by Author: "Spain"

9. **Query** [AQ8] : Please provide missing city for the [85] references list entry.
Response by Author: "Spain"

10. **Query** [AQ9] : Please provide missing Editor names, conference date, publisher name and city for the [97] references list entry.
Response by Author: " García-Lodeiro I, Fernández-Jiménez A, Blanco-Varela M, Palomo A. Synthesis and characterization of cementitious gels (C–S–H and N–A–S–H). Compatibility studies. In: Villanueva FJ (ed.), Proceedings of the 13th International Congress on the Chemistry of Cement (13th ICCC), 3–8 July 2011, Fundación CIEC, Madrid, Spain."

11. **Query** [AQ10] : Please provide missing Editor names, conference date, publisher name and city for the [102] references list entry.

Response by Author: "Glukhovsky VD. Ancient, modern and future concrete. In: Krivenko PV (ed.), Proceedings of the 1st International Conference on Alkaline Cements and Concretes, 11–14 October 1994, VIPOL Stock Company, Kiev, Ukraine. p. 53–62."

12. **Query** [AQ11] : Please provide missing city for the [114] references list entry.

Response by Author: "UNE-EN 197-1:2011. Spain"